applied sciences

MDPI

Article

An Explosive Driven Shock Tube-Based Laboratory Scale Test for Combined Blast and Fragment Impact Loading

Oussama Atoui [1,2,*], Georgios Kechagiadakis [2], Abdelhafidh Moumen [2,3], Azer Maazoun [4], Bachir Belkassem [2], Lincy Pyl [1] and David Lecompte [2]

[1] Mechanics of Materials and Constructions Department, Vrije Universiteit Brussel (VUB), Pleinlaan 2, 1050 Brussels, Belgium; lincy.pyl@vub.be
[2] Royal Military Academy, Civil and Materials Engineering Department, Avenue de la Renaissance 30, 1000 Brussels, Belgium; george.kechagiadakis@dymasec.be (G.K.); abdelhafidh.moumen@vki.be (A.M.); bachir.belkassem@hotmail.com (B.B.); david.lecompte@mil.be (D.L.)
[3] Environmental and Applied Fluid Dynamics Department, von Karman Institute for Fluid Dynamics, Chaussée de Waterloo 72, 1640 Rhode-Saint-Genèse, Belgium
[4] Civil Engineering Department, Defense Science and Technology, Military Research Center, Ministry of National Defense, Nabeul 8021, Tunisia; azer.maazoun@ugent.be
* Correspondence: oussama.atoui@vub.be; Tel.: +32-465-435-249

Abstract: This work is a part of a larger research effort to better understand the combined effect of the blast wave and fragment impacts following the detonation of a shrapnel bomb. It is known that the time interval Δt, which represents the difference in arrival time between the blast wave front and the fragment at the position of a given target object, has a significant influence on its response mode. This paper presents insights into the establishment of a laboratory scale technique to generate a combined blast loading and single or multiple projectile impacts on a target. The objective of the setup is to control the time interval Δt to a certain extent so that the different response modes of the tested structures can be investigated. In order to reduce the complexity associated with the random nature of the shrapnel, steel ball bearings are used to simulate the projected fragments. They are embedded in a solid explosive charge, which is detonated at the entrance of an explosive driven shock tube. The experimental work demonstrates that it is possible to orient the path of a single projectile inside the tube when aiming at a target positioned at its exit. The setup guarantees the generation of a well-controlled planar blast wave characterized by its peak pressure, impulse and blast wave arrival time at the exit of the tube. The influence of the mass of the charge and the diameter of the projectile on its velocity study shows that for the same charge mass, the time interval increases with increasing projectile diameter. The experiments are numerically simulated based on an Eulerian approach using the LS-DYNA finite element software. The computational model allows to reveal details about the projectile flight characteristics inside the tube. Both the experimental and numerical data show the influence of the charge and projectile parameters on the time interval.

Keywords: combined blast-fragment loading; time interval; computational model; explosive driven shock tube; improvised explosive device; projectile flight trajectory

Citation: Atoui, O.; Kechagiadakis, G.; Moumen, A.; Maazoun, A.; ; Belkassem, B.; Pyl, L.; Lecompte, D. An Explosive Driven Shock Tube-Based Laboratory Scale Test for Combined Blast and Fragment Impact Loading. *Appl. Sci.* **2022**, *12*, 6854. https://doi.org/10.3390/app12146854

Academic Editor: Genevieve Langdon

Received: 21 June 2022
Accepted: 2 July 2022
Published: 6 July 2022

1. Introduction

In May 2020, over 264 incidents of explosive violence around the world, resulting in 1573 deaths and injured victims, were recorded in the English language media worldwide [1]. In today's society, the threat of terrorism is ever present. The number of terrorist attacks using Improvised Explosive Devices (IED) has increased [2], targeting both civilians and military personnel in many places but especially in high-density public areas such as airports, concert arenas, security check-points, and public transport stations. Shrapnel bombs, pipe bombs or nail bombs, which are very often used in terrorist attacks, pose a serious threat to people and structures in the vicinity of the detonation. They are easy to manufacture and differ significantly from conventional munitions and cased charges.

Their lethality is based on both the velocity of the projected fragments and the intensity of the blast wave.

A shrapnel bomb is often referred to as an IED based on Home Made Explosives (HME) combined with a collection of metallic parts such as nails, screws, bolts and other randomly shaped fragments. They are used to increase the harmful effect on surrounding human and material targets. On detonation, a shrapnel bomb can result in three types of loadings: (i) a sudden pressure increase, (ii) multiple fragment impacts, and (iii) a combined loading caused by both the blast wave and the fragments' impact. The assessment of this combined loading is challenging. Therefore, blast and fragment impact loading are commonly treated separately in the design of protective structures. Previous studies [3,4] showed that in a realistic detonation scenario, a synergetic effect exists, resulting from the combination of blast loading and fragment impacts. More explicitly, this means that the structural response caused by the combined effect of blast and fragments is more severe than the sum of the responses caused by the separate actions of both loadings. Moreover, the arrival time of the blast wave front and the fragments at the targeted structure is different. This is due to the different velocities of both loadings and the distance between the charge and the structure. At short stand-off distance (SOD), the blast wave front travels faster than the fragments. As of a certain distance, the fragments will strike the structure first due to the faster decay of the blast wave velocity.

With the aim of reducing the combined effect of blast wave and fragment impact, two important challenges exist. The first challenge resides in the conception and design of protective (anti-blast and anti-fragment) materials and structures. The second one resides in how to accordingly test their combined ballistic and explosive protection level. On the one hand, different international ballistic standards are available to test structures under only fragment impact loading [5,6]. On the other hand, standards and testing methods to test structures under only blast loading are available as well [7–9]. However, few techniques are established for testing structures under the combined effect of blast wave and fragment impact loading [10–12]. Trying to simplify an actual shrapnel bomb test and maintain its repeatability, is a challenge. Mastering the different parameters that govern the synergetic effect of the blast wave and the fragment impact is required. An in-depth understanding of the phenomena accompanying the momentum transfer from the explosive to the fragments is needed. Therefore, the simplified test to be designed needs to accurately represent the influence of charge and projectile parameters on the dynamic behavior of the target.

A number of research efforts addressing this issue have been reported. Sipei et al. [13] experimentally investigated the different failure mechanisms of a sandwich panel under combined blast and fragment impact loading. The combined loading was generated using prefabricated cemented tungsten carbide fragments attached to the bottom surface of a cylindrical explosive charge. Results showed that, after the detonation, the propelled fragments impact the front surface of the panel at different velocities, angles of impact, and arrival times. The latter was found to be an influencing parameter in the initiation and the propagation of failure mechanisms in the different layers of the panel. It was also shown that the difference between the arrival time of the blast wave front and the arrival time of each one of the fragments aggravates the final damage caused to the multi-layered panel. Grisaro et al. [14] suggested a simplified approach using experimental case studies to investigate the influence of the arrival time of blast and fragments on the dynamic response of a reinforced concrete (RC) element. Results showed that for both short and larger stand-off ranges, the fragment impacts and their arrival time with respect to the blast wave must be considered.

Nyström et al. [15] investigated the detonation of bare charges next to heavy fragments. The fragments were projected onto reinforced concrete targets. It was shown that this technique of generating a combined loading highly influences the way in which the structure responds. They concluded that this is related to the difference in arrival time between the blast and the fragments at the target. Zhang et al. [16] supported the same conclusions. They demonstrated that the time interval Δt alters the dynamic behavior of the tested RC beams from low spallation to severe spallation or breach. Li et al. [17] demonstrated that, in addition to Δt, both the SOD and the explosive charge mass have a significant influence on the RC slab damage mode. Lai et al. [18] numerically investigated the damage caused to a storage tank subjected to the coupling effect of blast wave and fragment impact loading. The simulation results revealed that both the scaled distance and the arrival time of the fragment affect the storage tank damage. Price et al. [19] numerically investigated blast-driven fragments resulting from the detonation of spherical, cylindrical, and disk-shaped C4 explosive charges when projected inside a cylindrical tube. Although their computational model was able to predict the acceleration and the velocities of the blast-driven fragments, little focus was given to the influence of Δt on the dynamic behavior of the target. A more recent work by Lang et al. [20] addressed this topic. They proposed a laboratory technique which uses a composite projectile to simulate combined blast and single fragment impact loading on an Aluminum target. They showed that Δt has a significant influence on the response mode of the Aluminum plate (plugging, dishing, cracking, etc.). Qi et al. [21] shifted the focus and proved both experimentally and numerically the influence of charge shape and geometry on the velocity characteristics of an explosively driven single ball bearing and consequently on Δt. They further investigated the momentum transfer mechanism from the charge to the projectile.

These studies on the dynamic behavior of different materials and structures under the combined effect of blast wave and fragment impact loading improve our understanding of (i) the resistance of the different targets with respect to the combined loading, (ii) how the combined loading can be generated, and (iii) how the structures can be tested. The present paper studies the influence on Δt of the charge and the fragments characteristics (charge mass, projectile mass) and the stand-off distance from the center of the detonation to the target. Moreover it indicates how to establish a computational model in an attempt to better understand the momentum transfer from the charge to the projectile and its influence on Δt.

The present work is a part of a larger research effort to design a laboratory scale experimental technique to generate a reproducible combined blast and single or multiple fragment impact loading. The proposed test method is based on the use of small steel spheres embedded in a solid explosive, which is detonated at the entrance of an explosive driven shock tube (EDST). Optical techniques are used to capture the shock wave front, the projectile path, and the arrival time of both on the target.

The paper is organized as follows. In Section 2, the proposed laboratory technique to generate the combined loading is introduced. To this end, two main steps are undertaken. First, the blast, the projectile characteristics, and the time interval are investigated. Second, a case study application, where the combined effect of blast wave loading and projectile impact is applied on an Aluminum plate, is presented. In Section 3, a finite element (FE) model based on an Eulerian formulation using LS-DYNA [22] is proposed. The model is used for the study of the influence of the charge mass and the projectile diameter on the fragment velocity and on Δt. The numerical simulation results are then discussed and compared to the experimental output. Section 4 presents the conclusions.

2. Experimental Setup Using the Explosive Driven Shock Tube

2.1. Description of the Experimental Setup

HME are improvised, they are extremely diverse in design and can come in many forms, ranging from a small pipe bomb (practical option for terrorists) to a sophisticated device capable of causing massive damage to people and infrastructure [23]. Most of IEDs used in terrorist attacks are either spherical or cylindrical in shape. The enhancements added to the explosive charges differ in mass, shape, and geometry from one configuration to another. The full range of possibilities in the shape and the mass of the charge, together with the geometry, shape and mass of the fragments is considered as one of the great difficulties in IED research [13,19–21]. Therefore covering the whole range of possibilities in a laboratory-scale experiment is not realistic. In this paper, the choice is made to use a spherical steel projectile with a variable diameter attached to the front surface of a spherical explosive charge. Steel spheres with diameters of 5, 7, and 8 mm are half buried into the radial center of the front surface of the charges. C4 explosive charge masses of 10, 20, and 30 g are positioned at the entrance of the EDST. This choice is made to cover a specific configuration range that usually observe in real scenarios. The EDST is based on a cylindrical steel tube with a length of 1200 mm, a wall thickness of 4.5 mm and an inner diameter of 168.2 mm. The tube is reinforced at its entrance, over the first 200 mm, with a second steel tube. The latter has a 4.5 mm thickness and an inner diameter of 193.7 mm. Steel fiber-reinforced concrete is used to fill the radial space between the two tubes [24]. It is used to strengthen the region where the highest pressures occur. The EDST is mounted on a steel structure to allow for a controllable height from the ground as shown in Figure 1a. A steel frame with dimensions of 1000 mm × 1000 mm × 15 mm is placed at the exit of the tube. It is rigidly fixed to the ground and has an opening of 300 mm × 300 mm as shown in Figure 1b. This opening will hold a witness plate that will be subjected to the combined effect of blast wave loading and projectile impact.

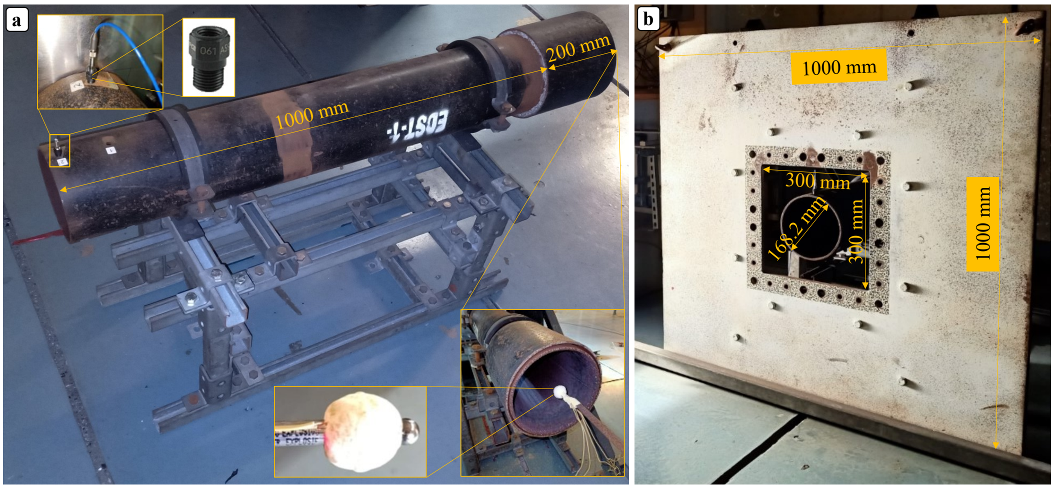

Figure 1. (**a**) EDST mounted on its controllable steel structure showing: (i) the placement of the C4 charge with the steel ball bearing at the tube's entrance, (ii) the high-frequency pressure sensor at the exit of the tube, (**b**) steel frame placed at the exit of the EDST to allow for the measurement of pressure, velocity, and arrival time.

A high-frequency pressure sensor [25] is placed at 20 mm from the exit of the EDST. It is used to record the incident pressure as well as the blast wave front arrival time. The pressure sensor is mounted on a special adaptor [25], which is used to attenuate the vibrations in the EDST wall resulting from the explosion. An image of the experimental setup showing all equipment is shown in Figure 2. An SA5 photron fastcam digital camera is positioned at a distance Z_c of 2350 mm from the center point of the tube. The camera is focused on a steel frame with plexiglas, which is positioned on the same optical axis at a distance Z_b of 1945 mm from the tube's center. A frame rate of 20,000 fps (frame per second) and a shutter speed of 6.42 µs are chosen together with a picture resolution of 704 × 520 pixels in order to measure the projectile velocity at the exit of the tube. A black and white speckle pattern, printed on a transparency film, is attached to the plexiglas [26]. Additionally, the speckle pattern is back-illuminated using two 575 W halogen lamps. A wall composed of thick rubber bricks is placed at a distance Y_w of 1885 mm from the tube's center. It serves to retain the steel spheres after the explosion and to record their impact points. The main aim is to extract conclusions concerning the projectile flight trajectory and the dispersion of impacts.

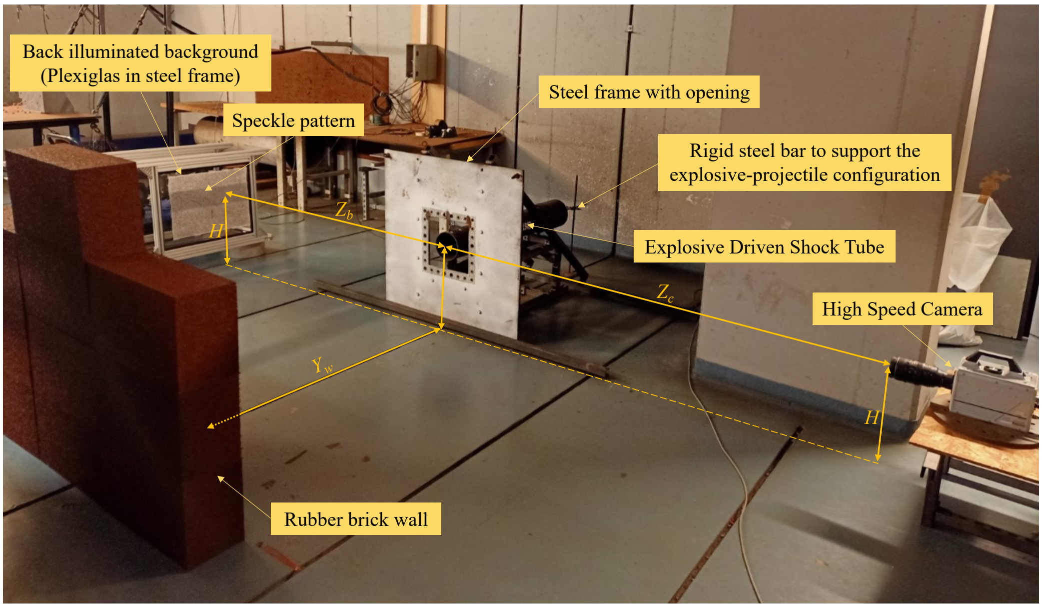

Figure 2. Image of the experimental setup using the EDST showing the instrumentation used to visualize the passage of the blast wave front and the projectile at the exit of the tube.

2.2. *Control of the Projectile Flight Trajectory*

In this phase, two main challenges are of concern. The first challenge resides in the capability of the propelled projectile to maintain an oriented on-axis path inside the tube from the moment of the detonation until impact on the target. The second challenge resides in limiting the dispersion of impacts on the witness plate. This will allow for a better reproducibility of tests. To this end, an experimental campaign is carried out which studies the flight trajectory of a projectile attached to a detonator and a rear-detonated C4 spherical explosive charge. In the following subsection, the details of the blast tests are presented.

2.2.1. Projectile Flight Trajectory and Dispersion of Impacts in Free Air

The experimental setup consists of nine polyurethane plates with dimensions of 1000 mm $\times$ 1220 mm $\times$ 50 mm attached to the same number of 80 mm thickness hardboard panels. They are arranged to form an octagon with a diameter of 2150 mm as shown in Figure 3. The polyurethane allows a good visibility of the projectile's impact point. A total of 23 tests are carried out [27]. A detonator and a rear-detonated C4 spherical explosive charge are used to accelerate the selected projectile. A distance of 910 mm separates the charge from the target. Steel spheres with diameters of 5, 7, and 8 mm are used. A steel bar is used for the fixation of the detonator-projectile configuration. An SA5 photron fastcam digital camera is positioned at a distance of 2150 mm from the center of the explosion. The HSC is configured with a frame rate of 50,000 fps and a shutter speed of 1/1,000,000 s^{-1}. A view from the top enables to track a part of the projectile's trajectory. Two 1500 W light emitting diodes are used to increase the illumination of the setup.

A typical result at different time steps of the flight trajectory of a 7 mm diameter projectile is shown in Figure 4. First, the projectile is accelerated by the blast wave generated by the explosive. The projectile's initial trajectory is hidden by the flash of the detonation. After its passage through the opaque gas cloud, the first appearance of the projectile is captured as shown in Figure 4a. A straight trajectory visualized by the yellow dashed line can be tracked. A straight trajectory can be seen as shown in the images corresponding to Figure 4b,c. At the end of its straight flight in the air, the position of the projectile impact on the target is recorded.

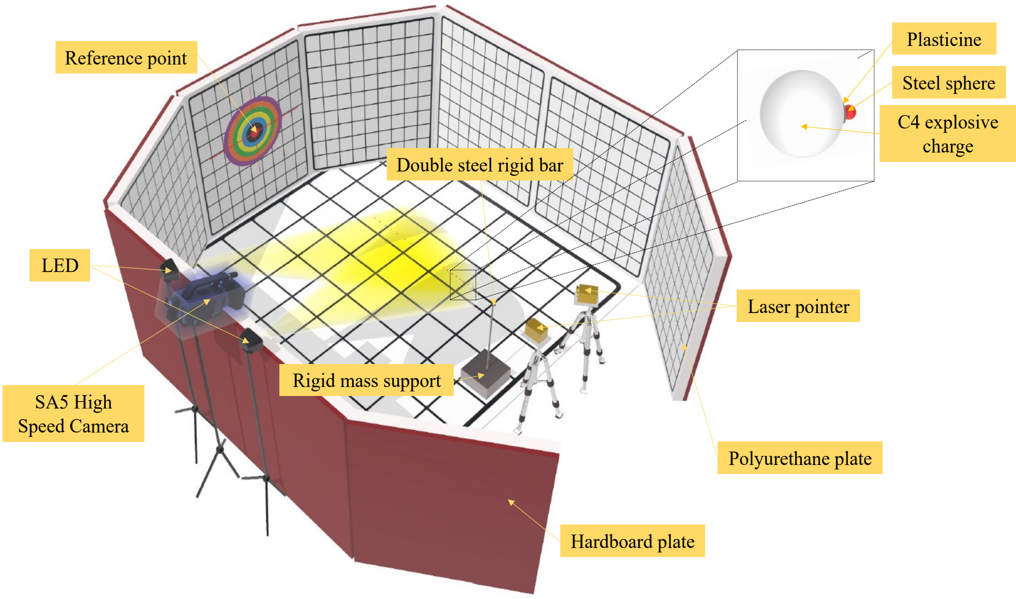

Figure 3. Schematic representation of the experimental setup showing the different instruments used to track the projectile flight trajectory.

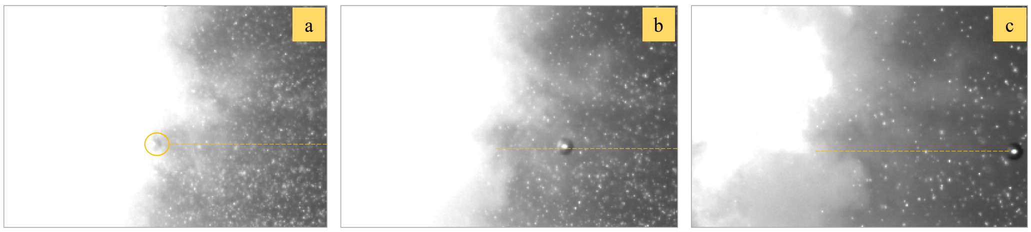

Figure 4. Typical flight trajectory of a 7 mm diameter projectile attached to the front surface of a detonator after being propelled by the explosion (Video S1): (**a**) first appearance of the projectile after its passage through the opaque gas cloud, (**b**) projectile's trajectory after detonation, (**c**) the projectile maintains a straight flight trajectory till impact on the target.

In a first step, the raw form of the projectile's position (in pixel per frame) versus time is extracted from the images. All the images are processed using an image processing software which enables the determination of the projectile's velocity. The fragment tracking software FTS developed at the Royal Military Academy of Brussels is used [28,29]. The tracking software uses images generated by a HSC to determine the displacement and the velocity data as function of time for a particular projectile during its flight. The coordinates of the impact points are recorded after each detonation. Figure 5 summarizes the dispersion of all impacts on the target. The area of all impacts is 100 mm × 100 mm. The dots represent tests where the projectiles hit the target in a single point. The special symbols, i.e., squares and diamonds, represent tests where the projectile respectively broke up into two and three parts due to the explosion itself.

In conclusion, the test campaign reveals two main results. The first resides in the capability of the projectiles to maintain an oriented path until impact on the target. The second is that the dispersion of impacts is circumscribed within an area which corresponds to the cross sectional area of the EDST. This means that the EDST can be used for further testing avoiding collision with the shock tube.

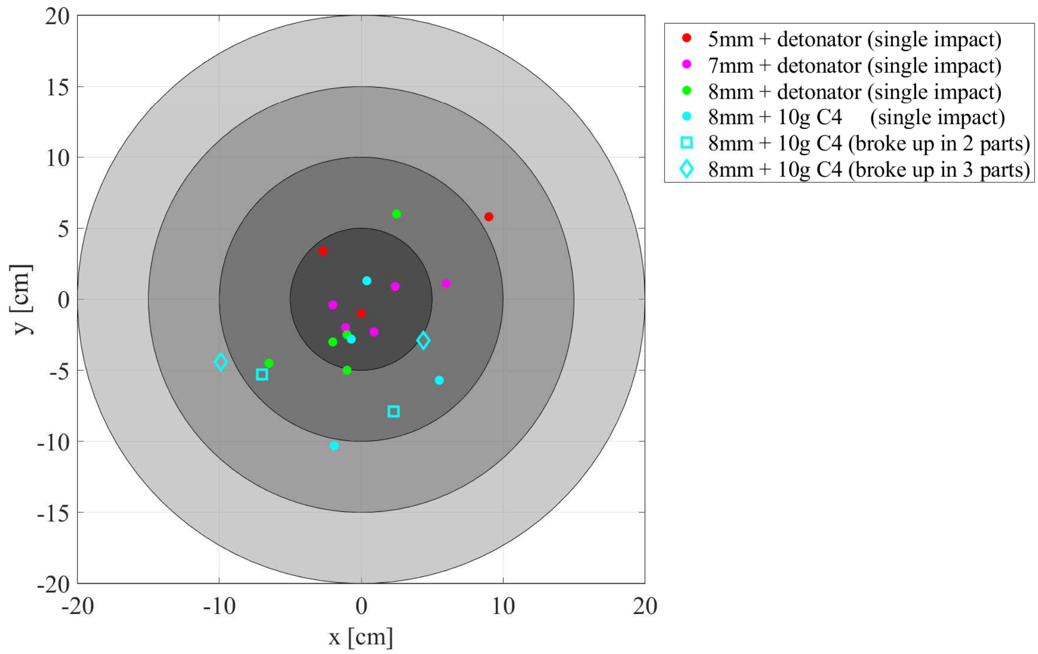

Figure 5. Representation of the dispersion of projectile impacts on the target using varying spheres (5, 7, and 8 mm) attached either to only a detonator or to a 10 g C4 spherical explosive charge.

2.2.2. Projectile Flight Trajectory and Dispersion of Impacts Using the EDST

In this phase, the setup of Figure 2 previously explained in Section 2.1 is used. The flight trajectory of 5 and 7 mm diameter projectiles propelled by 10, 20, and 30 g C4 explosive charges is tracked. It should be highlighted that a reproducible oriented path of the projectiles allows for a better extraction of their velocities, arrival times, and consequently Δt. For a better visualization of the passage of the blast wave front and the projectile in the field of view (FOV), images are processed using the particle image velocimetry (PIV) visualization technique [30]. This optical measurement technique is able, not only to provide quantitative data for the multiphase and transient characteristics of flows, but also to determine the spatiotemporal evolution of the shock wave and the projectile in all different flight phases.

A typical result from the high-speed camera HSC (Video S2) for the flight trajectory of a 7 mm diameter projectile propelled from the explosion of 10 g C4 at the entrance of the EDST is shown in Figure 6. The projectile is masked by a black circle. This allows to clearly distinguish its position in each frame. Images 1 and 2 in Figure 6 show the first and the last appearance of an almost plane blast wave front in the FOV, respectively. Image 3 represents the interference of reflected blast waves from the surrounding of the experimental setup. At an advanced time step after the passage of the blast wave, the projectile appears for the first time in the FOV. After that, as shown in images 4 to 6, an oriented trajectory can be tracked as visualized by the black dashed line from the exit of the tube till the end of the FOV. This straight path is maintained until impact of the projectile on the target. The images depict the magnitude of the displacement D (in pixel), which represents the distortion of the air density due to the passage of the shock wave. D is shown in colors where red represents the highest values. The main features of the flow field around the supersonic freely flying projectile, such as the spherical and the detached shock wave in its front, have been captured with a good spatial resolution. The position of the impact point is recorded after each detonation. It is found that in more than 92% of the performed experiments, the projectiles impact the target within an area of 165 mm $\times$ 165 mm as shown in Figure 7. The results are shown as a function of the different charge masses (10, 20, and 30 g C4) and projectile diameters (5 and 7 mm).

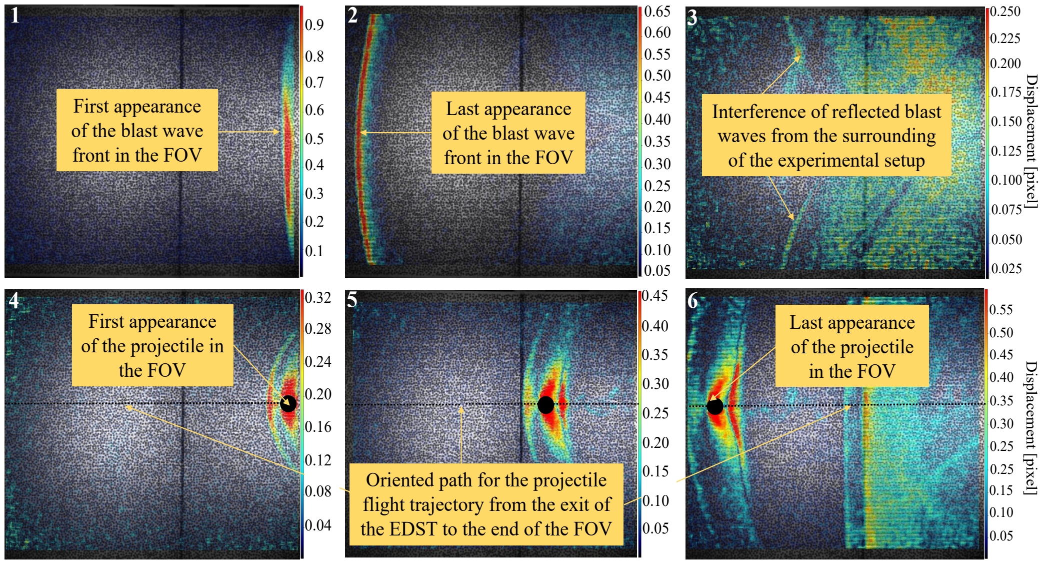

Figure 6. Images obtained from the HSC are processed using PIV technique and show an oriented path for the flight trajectory of a 7 mm diameter projectile: (i) images 1 to 3 represent the propagation of the blast wave in the camera field of view, (ii) images 4 to 6 depict the main features of the flow field around the freely flying projectile.

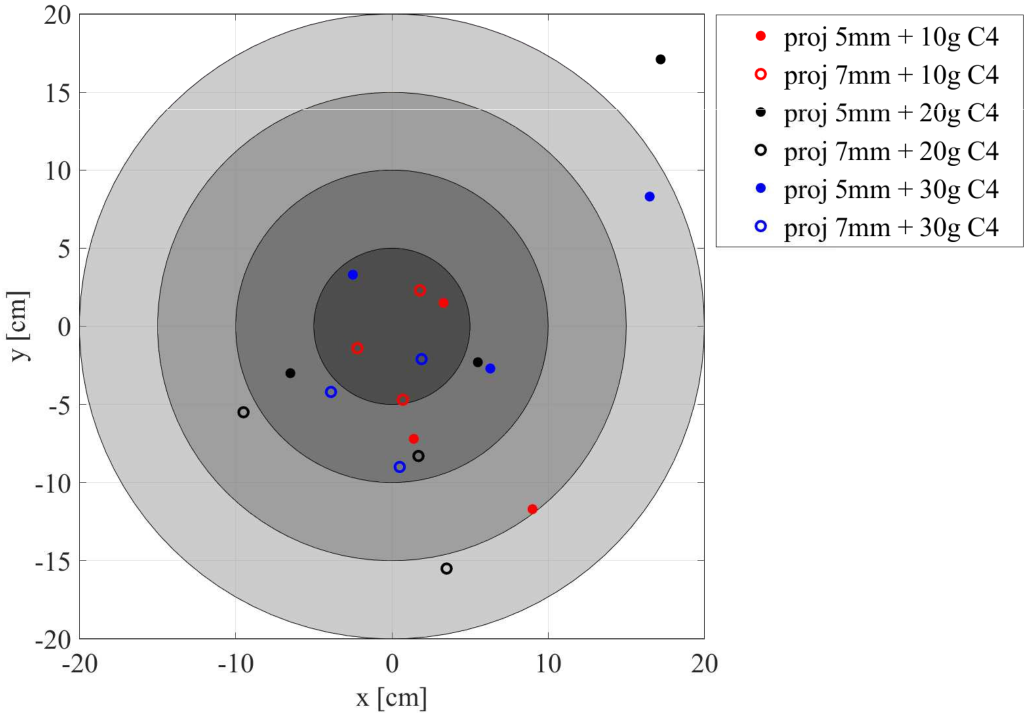

Figure 7. Representation of the dispersion of projectiles impacts using 5 and 7 mm projectile diameters and 10, 20, and 30 g C4 spherical explosive charges.

As a first conclusion, the experimental results reveal the capability of the different projectiles to maintain an oriented path from the moment of detonation until impact on the target. The different impacts lie within the cross-sectional area of the EDST.

2.3. Blast Loading Characteristics

In order to be a reliable laboratory scale technique, the setup also needs to generate a reproducible blast loading on the target structure. In what follows, the reproducibility of experiments in terms of pressure-time evolution and blast wave arrival time at the tube's exit, is investigated. Figure 8 represents the incident pressures as a function of time for C4 spherical explosive charge masses of 10, 20, and 30 g. Three tests are performed for each charge mass. Considering the noise in the measurements as a high-frequency signal, a Butterworth second-order low-pass filter is used in MATLAB. An average incident peak pressure of 778 kPa (in equivalent TNT) and an average arrival time of 0.84 ms are recorded for the 10 g C4 charge. For the 20 g charge tests, the peak pressure reaches an average value of 1207 kPa and a blast arrival time of 0.64 ms is recorded. An average incident peak pressure of 2107 kPa and an average arrival time of 0.54 ms are recorded for the 30 g C4 charge. The variability in the shock front arrival time of the initial shock wave together with the magnitude of the corresponding peak pressure are illustrated in Figure 9.

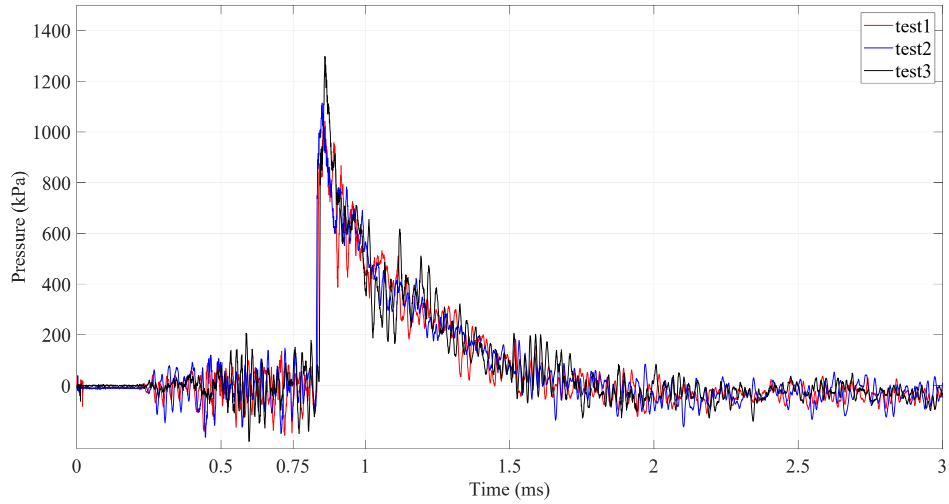

(**a**)

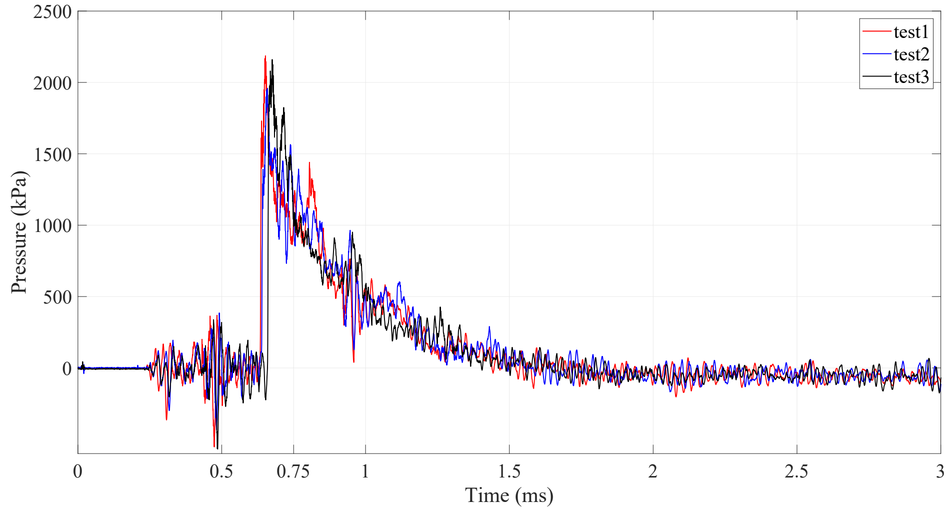

(**b**)

Figure 8. *Cont.*

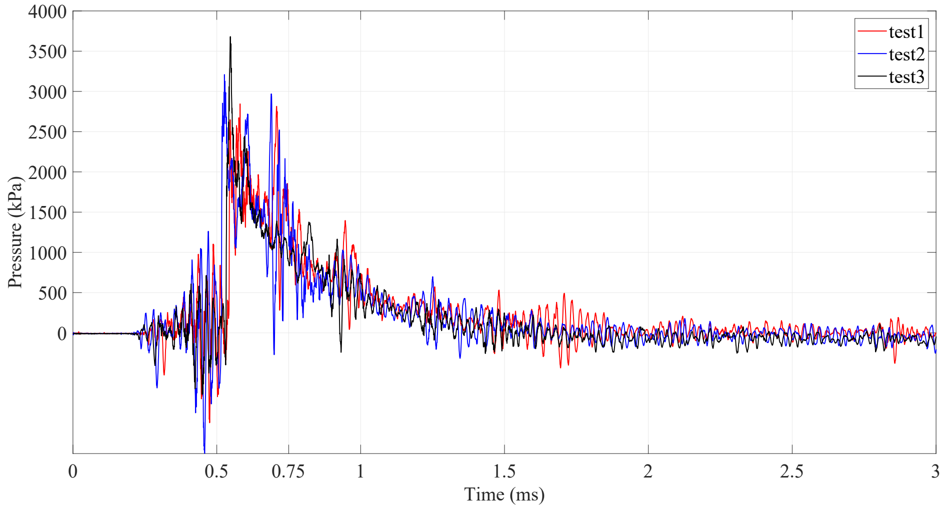

(**c**)

Figure 8. Pressure profile recorded by the high-frequency pressure sensor for the explosion of (**a**) 10 g, (**b**) 20 g, and (**c**) 30 g C4 charge masses.

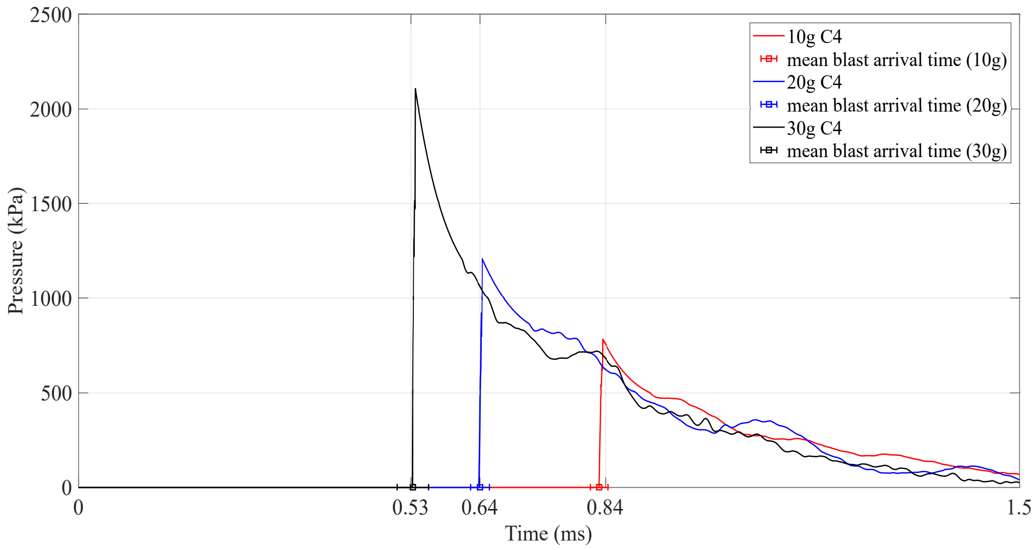

Figure 9. Average of the filtered signals of the pressure profiles for the 10, 20, and 30 g C4 charge masses and variability of the blast arrival time to the tube's exit.

In conclusion, the setup guarantees the reproducibility of the planar blast wave (magnitude and blast wave arrival time) applied on the target plate. The collected data will be compared to the results of the simulation in Section 3.

2.4. Projectile Characteristics

The focus is now on the projectile velocity at the exit of the tube. In order to extract the different velocities, again the in-house developed software FTS is used. The contrast and brightness parameters are defined such that the projectile is adequately isolated from its surroundings in terms of luminous intensity. The center of the projectile is then tracked and the displacement as a function of time is obtained. Consequently, the signal is derived so as to obtain the corresponding velocity of the fragment. Figure 10 shows the mean fragment velocity with standard deviation as a function of the charge mass. As expected, it can be observed that the C4 charge mass and the projectile diameter have an influence on its velocity. The 5 mm projectiles reach higher velocities than the 7 mm projectile for identical C4 charge masses. Figure 11 illustrates the percentage of energy ratio (projectile kinetic energy to charge energy) as function of charge masses. It is shown that the maximum energy ratio is obtained for the 7 mm diameter projectiles and decreases with increasing charge mass. This is not surprising knowing that the amount of transmitted energy is directly linked to the contact surface between the charge and the spheres. Moreover, an increase in the charge mass causes an increase in the charge volume. The latter causes the charge energy to increase and, consequently, a decrease in the energy ratio is obtained.

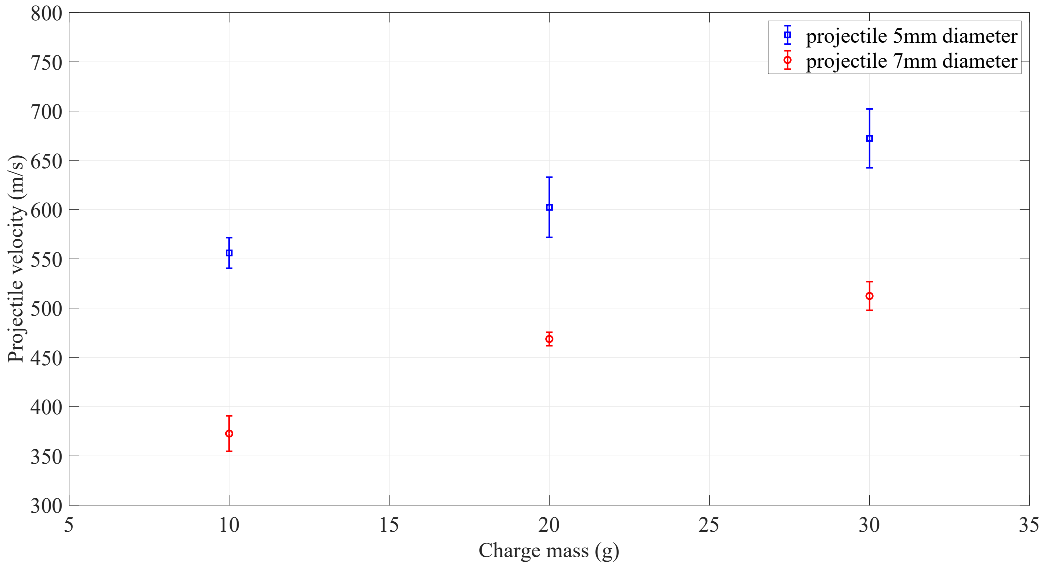

Figure 10. Mean projectile velocity with standard deviation for projectiles with diameters of 5 and 7 mm as a function of the charge mass.

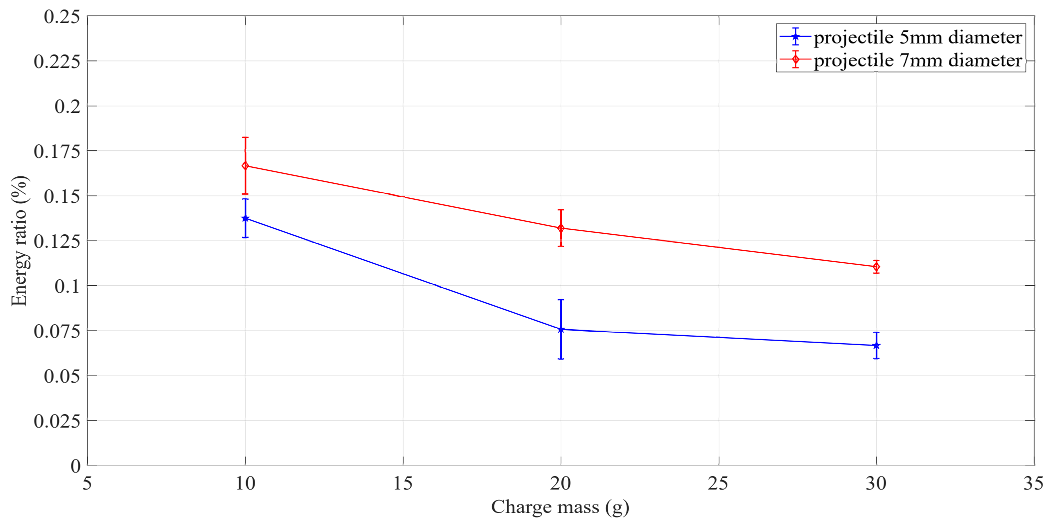

Figure 11. Percentage of energy transmitted from the charge to the 5 and 7 mm projectiles as function of charge mass.

2.5. Time Interval Δt

In this section, the time interval Δt is investigated. All images obtained from the HSC are processed using the photron fastcam viewer (PFV) [31]. The reference image is chosen as the last frame recorded immediately before the appearance of the blast wave in the FOV. In a first step, the position of the blast wave front d_{bl} after its first appearance in the FOV is determined as shown in Figure 12a. Then, its velocity v_{bl} is calculated. In a second step, the number of frames N_f between the first appearance of the blast wave front and the first appearance of the projectile in the FOV is registered. After that, the position d_p of the projectile is determined in the image in which it first appears as shown in Figure 12b. Its velocity v_p is obtained using the FTS as explained in Section 2.4.

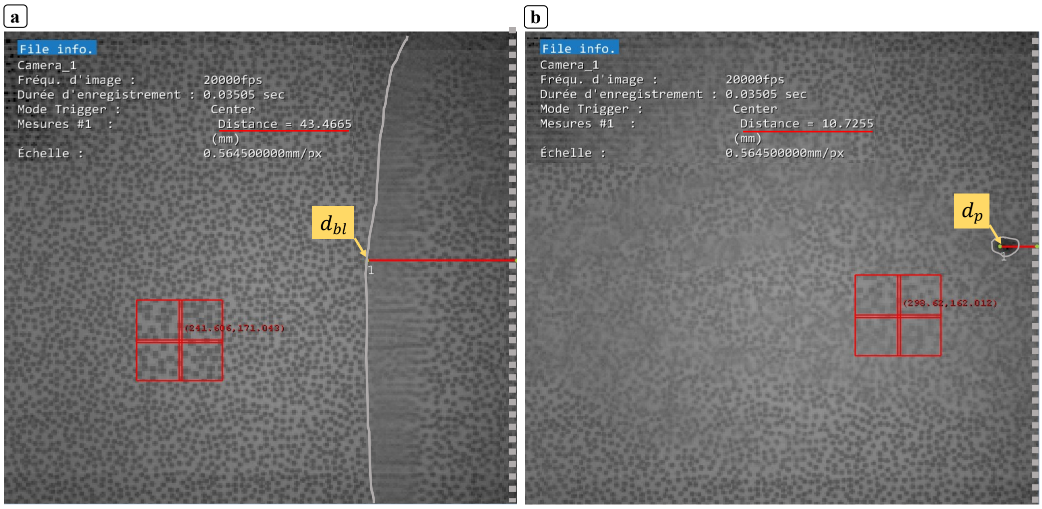

Figure 12. Extract from the PFV software for the measurements of: (**a**) position of the blast wave front after its first appearance in the FOV, (**b**) position of the projectile after its first appearance in the FOV. (See test 11 in Table 1).

Finally, the time interval Δt is obtained by applying Equation (1):

$$\Delta t = \left(\frac{N_f}{frame\ rate}\right) - \left(\frac{d_{bl}}{v_{bl}}\right) - \left(\frac{d_p}{v_p}\right) \quad (1)$$

Table 1. Values of the different parameters of Equation (1) for charge masses of 10, 20, and 30 g of C4 and 5 and 7 mm diameter of the projectile.

Test n	Charge Mass [g]	Projectile Diameter [mm]	N_f	d_{bl} [mm]	v_{bl} [m/s]	d_p [mm]	v_p [m/s]	Δt [ms]	Mean $\Delta t \pm \sigma$ [ms]
1	10	5	ND *	ND	ND	ND	ND	ND	1.21
2	10	5	27	32.74	925.78	19.76	533.21	1.27	
3	10	5	24	34.43	835.46	5.64	564.5	1.14	
4	20	5	23	53.62	1129.06	15.8	620.95	1.07	1.23 ± 0.23
5	20	5	24	48.54	1467.7	27.66	598.37	1.12	
6	20	5	31	35.56	1174.16	14.11	501.35	1.49	
7	30	5	24	31.61	1332.27	5.08	643.53	1.16	1.11 ± 0.04
8	30	5	24	66.04	1230.61	18.62	641.52	1.11	
9	30	5	22	21.45	1264.48	6.20	700.79	1.07	
10	10	7	43	29.91	880.62	16.38	383.86	2.07	2.14 ± 0.11
11	10	7	47	43.46	891.91	10.72	350.17	2.27	
12	10	7	44	47.98	890.21	15.25	361.28	2.1	
13	20	7	35	71.12	1264.48	14.68	440.31	1.66	1.70 ± 0.08
14	20	7	37	45.16	1230.61	6.79	474.18	1.79	
15	20	7	35	64.35	1117.71	11.85	463.02	1.65	
16	30	7	ND *	ND	ND	ND	ND	ND	1.62
17	30	7	32	80.72	1478.99	3.38	521.3	1.53	
18	30	7	35	20.88	1388.67	11.29	508.05	1.71	

* ND: No Data are obtained.

Table 1 summarizes all required values to obtain Δt for charge masses of 10, 20, and 30 g of C4 and both projectile diameters. It is highlighted that for the same charge mass, Δt increases with increasing projectile diameter. It is found that challenges exist in recording and analyzing data, including the short load duration, the high pressures, triggering challenges, and the bright explosive flash. Despite of these challenges, the versatility and the efficacy of high-speed imaging used in the experimental setup for visualizing the blast wave front and the projectile are of interest [32].

2.6. Combined Effect of Blast Wave and Projectile Impact Loading on a Plate: Case Study Application

As a proof of concept, two aluminum plate specimens are placed at the exit of the EDST. They are subjected to the combined effect of blast wave and projectile impact loading. The plates with material grade EN AW-1050A-H24 and dimensions of 400 mm × 400 mm × 2 mm (Figure 13a) are fixed to the steel frame using a bolted steel clamping frame with dimensions of 400 mm × 400 mm × 3 mm (Figure 13b). A second SA5 high-speed digital camera lens is positioned on the top of the rubber brick wall as shown in Figure 13c.

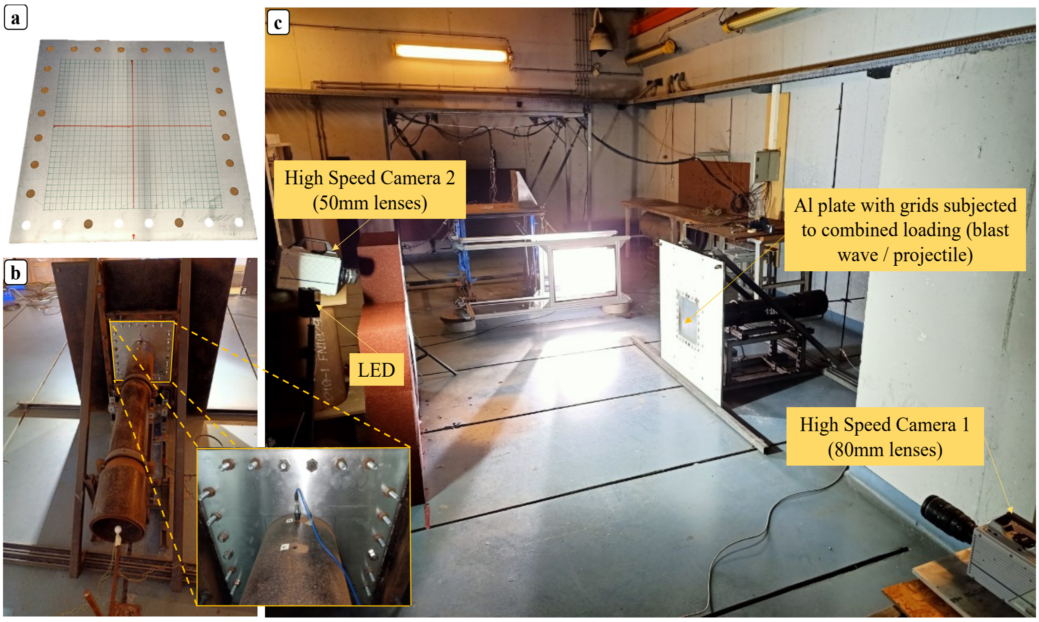

Figure 13. (**a**) Front face view of the Al plate target showing the grid, (**b**) Al plate positioned at the exit of the EDST and fixed to the steel frame, (**c**) image showing the position of HSC2 in the setup.

Images from HSC2 show: (i) the plate deformation at different time steps resulting from the explosion of 10 g of C4 at the entrance of the EDST and, (ii) the position of the projectile's impact point on the plate. Three different stages can be distinguished as shown in Figure 14a.

In the first stage, an out-of-plane displacement is observed in an area corresponding to the cross-section of the EDST (image 1). In a second stage, the motion propagates toward the edges of the plate. In a third stage, the plate reaches its maximum displacement. At this final stage, the projectile fully perforates the plate near its center (image 3). The position of the projectile's impact point in the plate, as shown in Figure 14b, gives insights about its trajectory inside the tube as discussed in Section 2.2.2. After perforation, the projectile is deformed and no longer spherical. The rear half side of the projectile, which was in contact with the spherical explosive charge, has darkened due to the fire ball. The front half side is slightly flattened due to the impact of the plate. Images of the 7 mm diameter projectiles for the two tests of 10 g of C4 detonated at the entrance of the EDST are shown in Figure 14c.

In conclusion, the experimental study carried out in this work led to the establishment of a laboratory scale technique to generate a repeatable combined blast loading and single projectile impact on a target. The setup guarantees the stability and the on-axis trajectory in the different phases of the spherical projectile's flight. Moreover, the setup guarantees the repeatability of a planar blast wave (magnitude and blast wave arrival time) applied on the target plate. Finally, the setup is capable to a certain extent of controlling Δt based on the mass of the charge and the diameter of the steel spherical projectile.

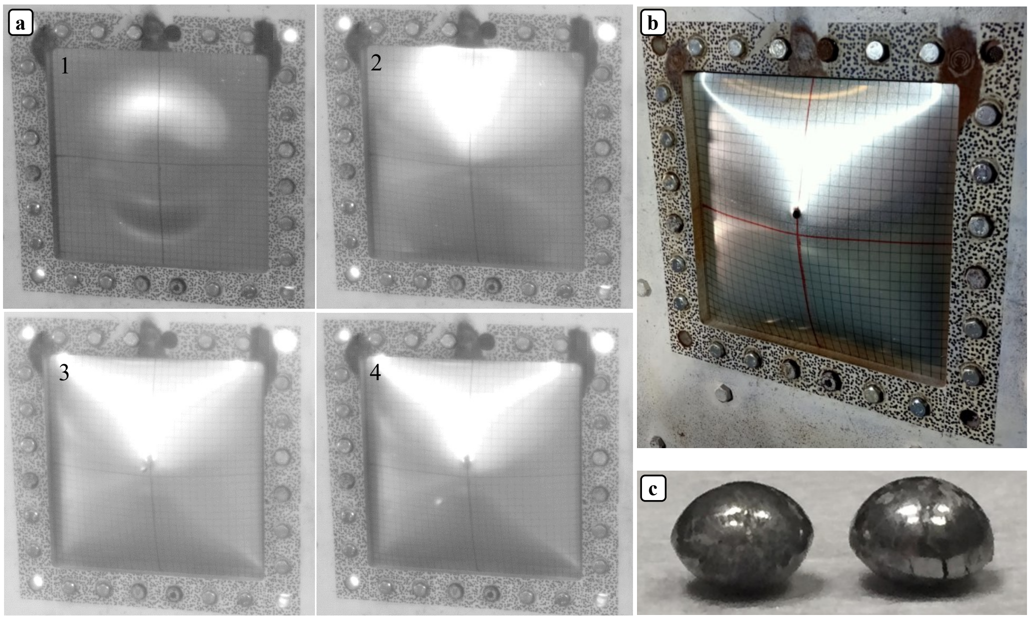

Figure 14. (**a**) Images from HSC2 showing the plate deformation at different time steps and the projectile perforation resulting from the explosion of 10 g of C4 at the entrance of the EDST (Video S3), (**b**) projectile impact point in the plate giving insights about its trajectory inside the EDST, (**c**) features of the projectiles after testing.

3. Computational Modeling

3.1. Formulation Approach

In the present study, the Eulerian approach is adopted. The Eulerian method has been widely used in simulating explosion problems [33–35]. It is applicable to 2D configurations and has proven useful to obtain comparatively good results at a moderate CPU cost [36]. Additionally, it has potential for simulating the basic hydrodynamic mechanisms of gas-solid flow behavior such as particle trajectory and particle velocity.

3.2. Model Setup

The aim of the numerical simulation explained in this section is to predict the pressure profiles, the blast arrival time, the projectile velocity, and the different phases of the projectile flight. The model will additionally serve to investigate other scenarios that were not performed experimentally. To this end, the explicit solver of the nonlinear finite element code provided by LS-DYNA is used. It takes into account both material and geometric nonlinearity. The FE model is constructed using the geometrical characteristics detailed in the experimental arrangement shown in Figure 15. Taking into account (i) the sphericity of the explosive charge and the projectile, (ii) the circular form of the cross-sectional area of the EDST, and (iii) the axi-symmetric geometry of the tube, a 2D axi-symmetric purely Eulerian model is adopted.

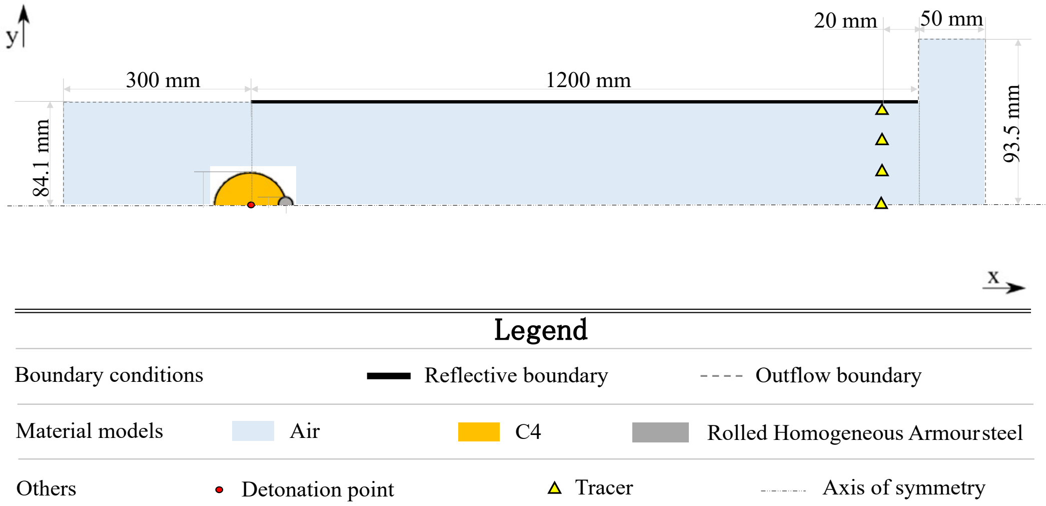

Figure 15. Schematic representation of the 2D axi-symmetric model in LS-DYNA: geometry, dimensions, materials, and boundary conditions.

3.2.1. Geometry and Boundary Conditions

It should be highlighted that the dynamic behavior of the Aluminum plate under the combined effect of blast wave and fragment impact is out of scope for the present numerical study and will be addressed in future work. Consequently, only the EDST, the air, the explosive charge, and the projectile are modeled. The tube wall is modeled as a perfectly reflective and rigid wall. Therefore, it is simulated by constraining the flow in the Arbitrary Lagrangian Eulerian ALE mesh in the normal direction of the 1200 mm edge elements. The segments selected in the wall of the EDST were set as "no flow through normal direction" using *ALE essential boundary of the *ALE card. An "outflow" of 300 mm is considered at the entrance of the EDST where the spherical explosive charge is detonated. There were no set conditions on the segments of the free air mesh at the entrance of the tube. The total meshed area has dimensions of 1550 mm by 93.5 mm. At the tube's exit, an outflow of 50 mm by 93.5 mm is considered. It serves to simulate the environment where the projectile enters in contact with free air. The detonation is set at time zero and located in the center of the explosive charge.

A mesh convergence study is conducted to determine an adequate mesh size. It is important to choose a mesh size that allows to adequately simulate the explosive energy release. Additionally, it has to accurately capture the blast wave front at the tube's exit. The pressures as a function of the inverse of the mesh sizes were recorded for mesh sizes ranging from 4 mm to 0.25 mm. Results reveal that convergence is obtained as from a 0.5 mm mesh size. This optimal mesh size also fits into the recommendation given by Schwer and Rigby [37] for the simulation of energy release.

3.2.2. Material Formulation

There are three parts to consider: air, explosive, and the projectile. As far as the air and the explosive are concerned, two equations must be defined. They require each a material model and an equation of state (EOS). The air is considered as an ideal gas and is modeled using (*MAT-NULL). The latter allows an EOS to be used without computing the deviatoric stresses [22]. Therefore, the gamma law EOS, given by Equation (2), with the keyword (*LINEAR-POLYNOMIAL) is used.

$$P = C_0 + C_1\mu + C_2\mu^2 + C_3\mu^3 + (C_4 + C_5\mu + C_6\mu^2)E \tag{2}$$

The parameters C_0, C_1, C_2, C_3, C_4, C_5, and C_6 are constants, $\mu = (\rho/\rho_0) - 1$, ρ is the current density, ρ_0 is the initial density having a value of 1.225 kg.m^{-3}, E refers to the specific internal energy. By setting $C_0 = C_1 = C_2 = C_3 = C_6 = 0$, and $C_4 = C_5 = \gamma - 1$, the ideal EOS is obtained.

$$P = (\gamma - 1)E(\rho/\rho_0) \tag{3}$$

γ represents the ratio of the specific heat for air and is equal to 1.4. The initial specific internal energy is set as E_0 = 0.2534 kJ.kg^{-1} to give an atmospheric pressure of 0.101325 MPa. The initial relative volume is set as V_0 = 1 [22]. The corresponding numerical parameters are collected in Table 2.

Table 2. Parameters for linear polynomial EOS for the air.

C_0	C_1	C_2	C_3	C_4	C_5	C_6	E_0 [kJ.kg^{-1}]	$V_0[-]$
0	0	0	0	0.4	0.4	0	0.2534	1

(*MAT-HIGH-EXPLOSIVE-BURN) is used for the C4 explosive material. The hydrodynamic behavior is given by the semi-empirical (*JONES-WILKINS-LEE) EOS in Equation (4).

$$P = A\left(1 - \frac{\omega}{R_1 V}\right)exp^{-R_1 V} + B\left(1 - \frac{\omega}{R_2 V}\right)exp^{-R_2 V} + \frac{\omega E}{V} \tag{4}$$

The parameters A, B, R_1, R_2, and ω are constants which depend on the type of explosive and which can be determined experimentally [38]. V is the volume and E is the specific internal energy. The Chapman–Jouguet pressure P_{cj} and the detonation velocity D_v are also needed to control the programmed detonation of the explosive. All values for the explosive properties and the EOS are taken as the parameters published by Dobratz and Crawford [39] and are summarized in Table 3.

Table 3. Explosive material properties and EOS parameters.

EOS-JWL						Mat High Explosive Burn		
A [GPa]	B [GPa]	R_1	R_2	ω	E_0 [kJ.kg^{-1}]	ρ [kg/m^3]	P_{cj} [GPa]	D_v [m/s]
609.77	12.95	4.5	1.4	0.25	9	1601	28	8193

It is experimentally observed that the projectile exhibits considerable deformation, especially during the initial blasting but with little effect on the inflight velocity characteristics. Taking this into account together with the fact that the projectile is made out of rolled homogeneous armored (RHA) steel, the (*SIMPLIFIED-JOHNSON-COOK) material model is used in the simulation. The general expression of the equivalent yield stress is given by Equation (5):

$$\sigma_{eq} = (A + B\epsilon^n)(1 + C\ln\frac{\dot{\epsilon}}{\dot{\epsilon_0}}) \tag{5}$$

where ϵ is the equivalent plastic strain, $\dot{\epsilon}$ is the strain rate, $\dot{\epsilon_0}$ is a reference strain rate. A, B, n, and C are the constant parameters for the material model. Table 4 summarizes the different mechanical parameters and the Johnson–Cook model constants for RHA steel.

Table 4. Density, elastic constants, and Johnson–Cook parameters for the RHA steel sphere [40].

	Property Name	Symbol	Value	Unit
Elastic constants	Mass density	ρ	7850	[kg/m^3]
	Young's modulus	E	1.97×10^5	[MPa]
	Poisson's ratio	ν	0.3	[-]
Johnson–Cook parameters	Yield stress	A	1225	[MPa]
	Strain-hardening constant	B	1575	[MPa]
	Strain-hardening coefficient	n	0.768	[-]
	Strengthening coefficient of strain rate	C	0.0049	[-]

3.2.3. Simulation Control Parameters

Some other parameters are needed to control the simulation. It is generally recommended to set the advection logic DCT to -1 when explosives are involved. When this value is set in the ALE control card, it corrects redundant out-flux at the corner elements of the material. Consequently, the negative volume problem is avoided. Moreover, it helps to remove several artificial constraints that are originally implemented in the advection to assist for the simulation's stability but are no longer needed after that. The advection method used for the calculation is the donor cell, first-order method accurate (METH = 3). In this advection method, the total energy is conserved over each advection step instead of the internal energy. This choice helps to preserve a better accuracy of the general shape of pressure waves. Moreover, it reduces the mesh bias by relaxing the monotonicity condition. Additionally, the smoothing is turned on by putting AFAC to 0. The environment pressure is considered as the atmospheric pressure and is set in the simulation by putting PREF to a value of 101,325 Pa.

3.3. Simulation Results

The performed numerical simulations cover a wider range of charge masses than considered in the physical experiments. The numerical results that overlap with the physical experiments are used to compare to the FE modeling predictions. The extra simulations (virtual experiments) are used to uncover details about the influence of the charge mass on the projectile velocity and, consequently, on the time interval. In the following, a total of fourteen 2D axi-symmetric simulations for 5 and 7 mm blast-driven projectiles embedded in rear detonated spherical C4 explosive charges (from 5 to 35 g) are performed. Table 5 summarizes the obtained numerical results.

3.3.1. Blast Wave and Projectile Flight Characteristics

After the detonation of the explosive charge, only part of the blast wave enters the tube. Multiple reflections occur till the formation of a planar blast wave. The planarity evolution is evaluated through a section of tracers at 400 mm, 800 mm, and 1200 mm from the point of detonation. To enable comparison with the experimental results measured by the pressure transducer, additional tracers are placed at 1180 mm. The results reveal that, for example, for the case of 30 g of C4 (simulation ID 12 in Table 5), a planar blast wave front begins to form at time 0.529 ms as shown in Figure 16. A graph of the projectile's velocity from the moment of detonation until its arrival to the tube's exit is presented in Figure 17. It is observed from Figure 17 that the projectile's flight path can be divided into four phases. The first phase starts at the moment of detonation initiation until the entire impulse transfer from the explosion to the projectile has completed. During this phase, the projectile accelerates to finally achieve a maximum velocity. In a second phase, a pressure decrease in the expansion gases surrounding the projectile causes the latter to cease accelerating. As of this moment, the projectile travels at constant speed. In a third phase, the reflected blast waves from the EDST walls interact with the projectile leading to a drop in the projectile's velocity. At 0.2 ms, the fourth phase is initiated and the projectile continues its flight accompanied with consecutive drops in velocity caused by the multiple interactions with the reflected blast waves. At time 2.01 ms, the projectile exits the tube at quasi constant velocity as shown in phase 4 of Figure 17. The same phases are discerned in all other simulations with differences in the projectiles velocities at the tube's exit.

Table 5. Table of values of the numerical simulations results for the pressures, time intervals, and projectile velocities and comparison with the blast and fragment impact tests.

Simulation ID	Simulation Inputs			At 1180 mm from the Center of Detonation						At 1200 mm from the Center of Detonation							
	Charge Mass (g)	Charge Diameter (mm)	Projectile Diameter (mm)	$t_{A/blast}$ (ms)			Peak Pressure (MPa)			$t_{A/blast}$ (ms)	$t_{A/proj}$ (ms)	Time Interval Δt (ms)			Projectile Velocity (m/s)		
				Num	Exp	Relative Error (%)	Num	Exp	Relative Error (%)			Num	Exp	Relative Error (%)	Num	Exp	Relative Error (%)
1	5	18.12	5	1.24	*VE		0.32	*VE		1.28	2.22	0.94	*VE		536	*VE	
2			7	1.24			0.34			1.28	3.04	1.76			388		
3	10	22.84	5	0.90	0.84	+7.14	0.61	0.78	−21.59	0.92	1.90	0.98	1.21	−19.10	632	549	+15.22
4			7	0.91	0.84	+8.33	0.60	0.78	−22.21	0.96	2.56	1.60	2.14	−25.23	465	365	+27.40
5	15	26.14	5	0.75	*VE		0.87	*VE		0.78	1.76	0.98	*VE		666	*VE	
6			7	0.78			0.88			0.80	2.34	1.54			505		
7	20	28.78	5	0.68	0.64	+6.25	1.15	1.21	−4.72	0.69	1.67	0.98	1.23	−20.32	703	573	+22.70
8			7	0.68	0.64	+6.25	1.13	1.21	−6.37	0.70	2.19	1.49	1.70	−12.40	538	459	+17.21
9	25	31	5	0.62	*VE		1.39	*VE		0.63	1.61	0.98	*VE		727	*VE	
10			7	0.62			1.38			0.64	2.09	1.45			562		
11	30	32.94	5	0.58	0.54	+7.40	1.64	2.11	−22.16	0.59	1.58	0.98	1.11	−11.71	739	662	+11.63
12			7	0.58	0.54	+7.40	1.62	2.11	−23.11	0.59	2.01	1.42	1.62	−12.34	579	514	+12.64
13	35	34.68	5	0.54	*VE		1.88	*VE		0.55	1.55	1.00	*VE		749	*VE	
14			7	0.54			1.86			0.56	1.97	1.41			593		

*VE: Virtual Experiment (no physical blast test was performed at this charge mass).

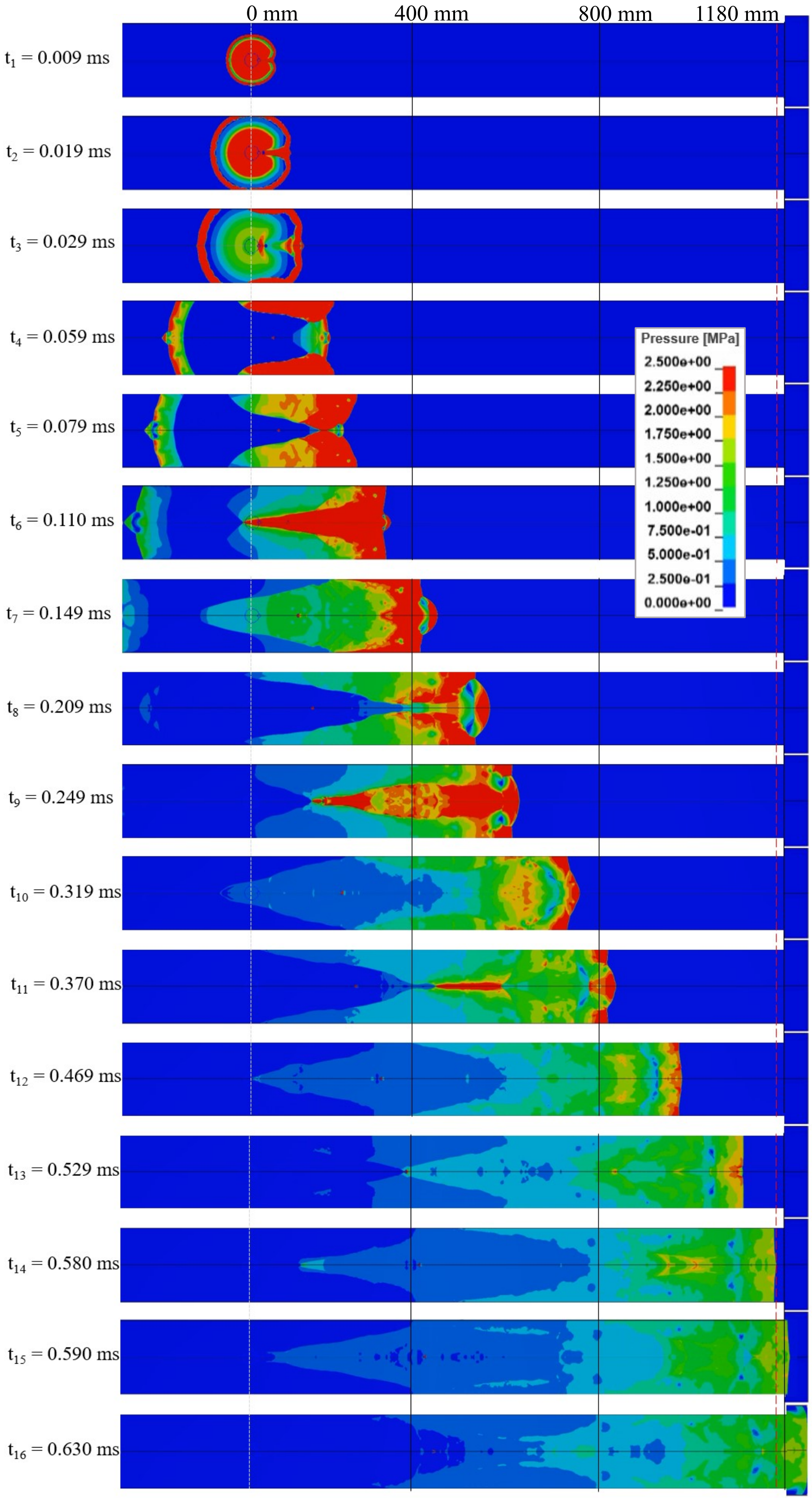

Figure 16. Propagation of a blast wave in the EDST (30 g C4 and 7 mm diameter projectile) (NB: the planarity of the blast wave front is checked via placing a section of tracers at 400 mm, 800 mm, 1180 mm, and 1200 mm from the detonation point).

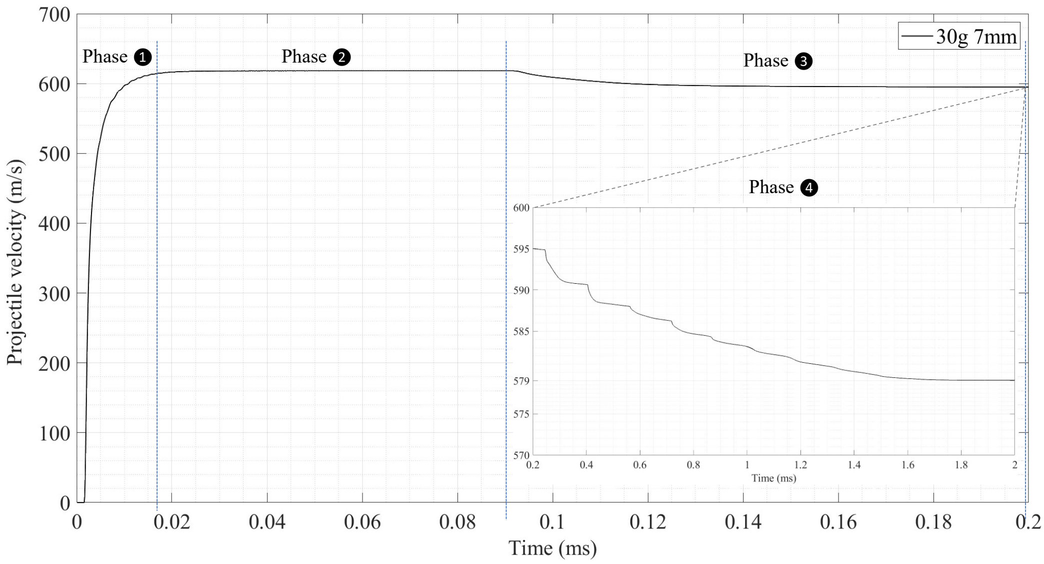

Figure 17. A graph of a typical projectile velocity evolution from the moment of detonation until its arrival at the tube's exit (case of 30 g of C4 and 7 mm projectile diameter).

3.3.2. Comparison between Experimental and Numerical Results

To further verify the reliability of the FE model, a comparison between the experimental and the numerical results is performed. Four variables are compared: the peak incident pressure, the blast arrival time, the projectile velocity at the tube's exit, and Δt. Figure 18 shows a comparison between experimental and numerical data of the TNT equivalent peak pressures and blast arrival times at 1180 mm from the center of detonation for 10, 20, and 30 g spherical explosive charges. The solid and dashed curves represent the experimental and numerical pressure–time history curves, respectively. The relative error in the peak overpressures obtained by FE model and the tests ranges between −23.11% and −4.72% while for the blast arrival time it ranges between +6.25% and +8.33%. The largest differences between the experiments and the simulations in blast arrival time and peak pressure are 60 µs and 0.46 MPa, respectively. Figure 18 shows that the simulation tends to under-estimate the peak pressure and over-predict the blast arrival time. This is not surprising knowing that the physics of the simulation is not fully able to capture the irregularity of the fire ball development inside the tube. The numerical pressure–time histories show a less sharp decay during the positive phase duration when compared to the experimentally recorded pressure profiles.

Figure 19 shows a comparison between experimental and numerical simulation results of the projectiles velocities at the tube's exit (1200 mm) for the detonation of 10, 20, and 30 g explosive charges. The solid and dashed curves represent the simulated projectile velocities as a function of time for 5 and 7 mm diameter projectiles, respectively. Each curve tip-end corresponds to the projectile arrival time to the tube's exit. Corresponding experimental results for the projectile velocities are given for 5 and 7 mm projectile diameter in terms of square and circle error bars, respectively. The relative error in projectile velocities obtained by the physical blast tests and the corresponding simulations ranges between +11.63% and +27.39%. This error margin is not surprising knowing that the parameters in the physical detonation such as projectile position in the charge, exact detonator position, charge surface irregularities and imperfect sphericity of the explosive charge are all ideally represented in the computational model.

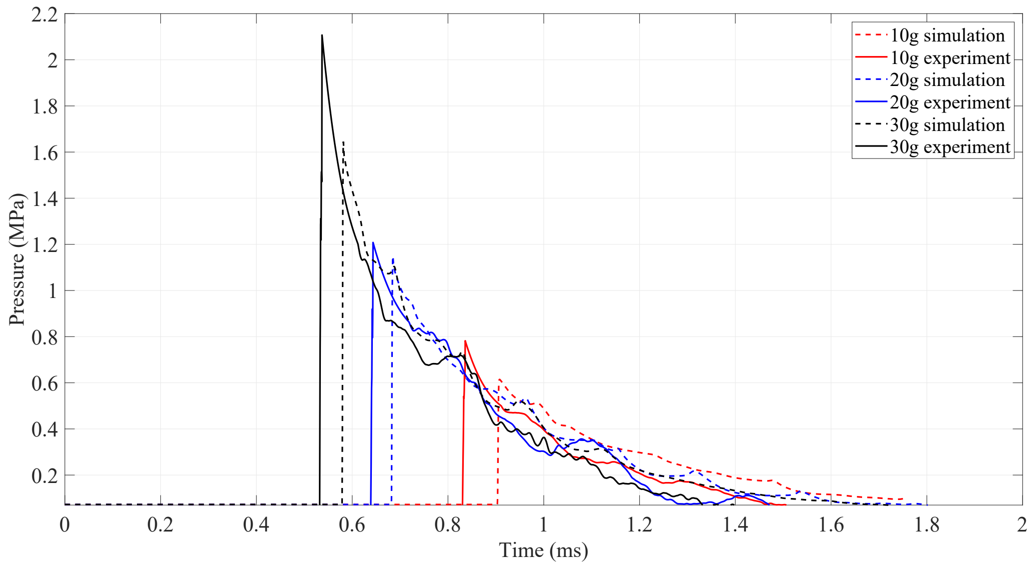

Figure 18. Comparison between experimental and numerical simulation results of the TNT equivalent peak pressures and blast arrival times at 1180 mm from the center of detonation for 10, 20, and 30 g spherical explosive charges.

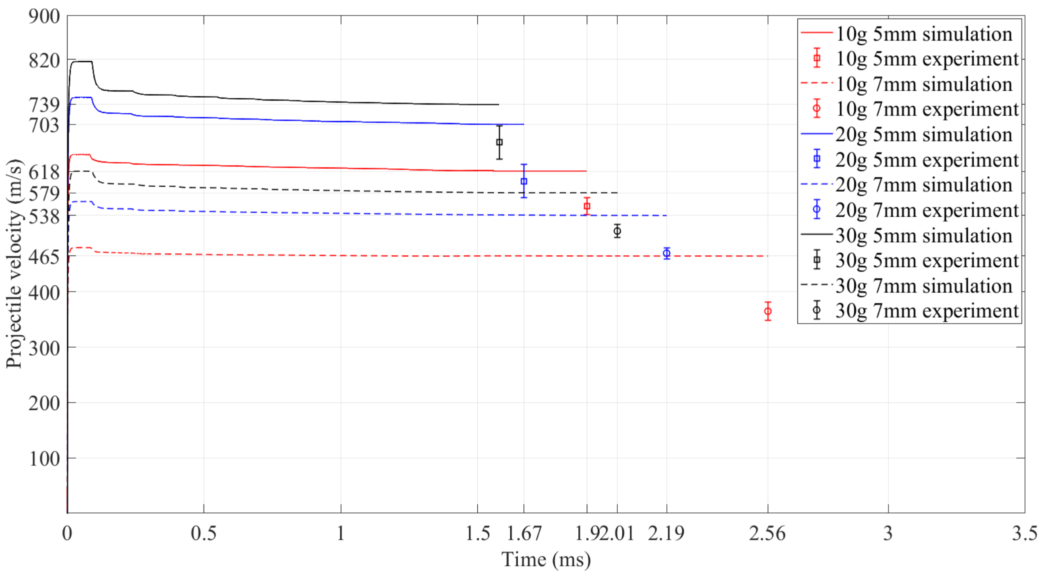

Figure 19. Comparison between experimental and numerical simulation results of the projectiles velocities at the tube's exit (1200 mm) for detonation of 10, 20, and 30 g spherical explosive charges and 5 and 7 mm projectile diameters.

Figure 20 shows the experimental and numerical simulation results of the time interval at the tube's exit. The mean Δt underestimation for the 5 and 7 mm diameter projectiles amounts to 17.04% and 16.64%, respectively. This error margin could be due to the limited capability of the simulation to reproduce the exact projectile's deformation resulting from the explosion. In the physical blast tests, it is found that some of the recovered steel spheres exhibited a mass reduction due to deformation and partial fragmentation. This means that the blasted samples gained additional velocity as compared to their numerical counterparts. The change in the projectile's velocity alters the projectile's arrival time to the tube's exit and consequently the time interval Δt.

In conclusion, a good agreement between the simulation results and the experimental data is found. The numerical model is able to reproduce the peak pressures, the blast and projectile arrival times, the projectile velocity, and the time interval.

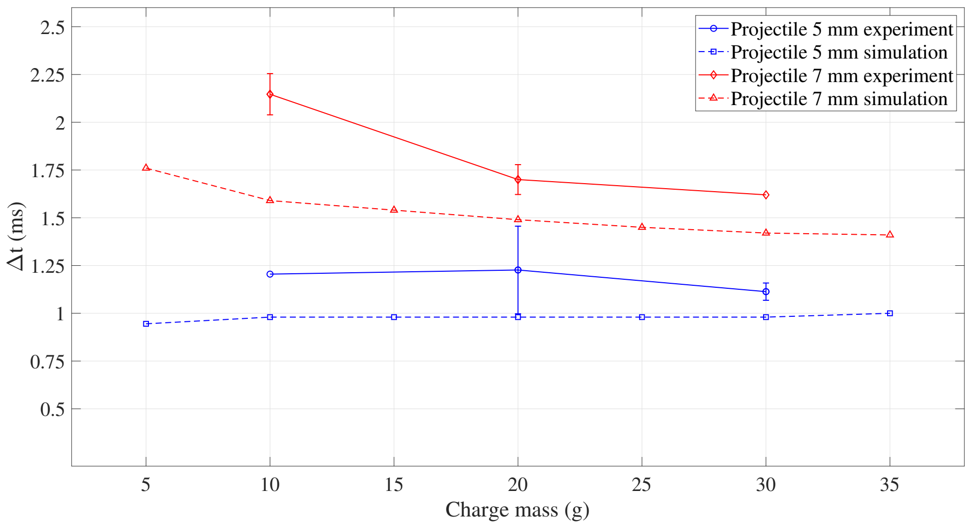

Figure 20. Comparison between experimental and numerical simulation results of the time interval Δt (shown by mean and standard deviation for experiments) at the tube's exit (1200 mm) for the different explosive charges and projectile diameters.

4. Conclusions

An experimental technique was developed to enable the study of a single spherical projectile propelled by the detonation of a spherical explosive charge using an EDST. The steel sphere was chosen to simulate an idealized piece of shrapnel from an improvised explosive device. In a first step, an experimental campaign was carried out to study the flight trajectory of a steel sphere in free air and the dispersion of impacts. The main aim was to examine the influence of charge mass and projectile diameter on projectile velocity and flight trajectories. In a second step, the spherical charge is detonated at the entrance of an explosive driven shock tube. Optical techniques using high speed cameras were applied to the blast test arrangement to visualize both the shock wave front and the projectile trajectory. Investigations on the blast loading characteristics, the projectile characteristics, and the time interval Δt have been performed. The different phases of the projectile flight were analyzed using an in-house developed fragment tracking software. As a proof of concept, a case study application where Aluminum plates were subjected to the combined effect of blast wave and projectile impact loading is presented. Finally, the experiments were numerically simulated based on an Eulerian approach using the LS-DYNA FE software.

The experiments revealed:

1. The capability of the steel spheres to maintain an oriented path in free air until impact on the target. The dispersion of impacts is circumscribed within an area which corresponds to the cross-sectional area of the used EDST.
2. The optical measurement technique is able to determine the spatiotemporal evolution of the shock wave and the projectile in all different flight phases.
3. The established laboratory scale technique is able to generate a repeatable combined blast and single projectile impact loading on the target.
4. The capability of the steel spheres to maintain an oriented path inside the explosive driven shock tube when aiming a structure placed at its exit and to limit the dispersion of impacts on the target.
5. The setup guarantees the reproducibility of a planar blast wave (magnitude and arrival time) applied on a target plate placed at the tube's exit. For the same charge mass, the time interval Δt increases with increasing projectile diameter.

The numerical work revealed:

1. The FE model is able to reproduce the peak pressures, the blast wave and projectile arrival times, the projectile velocity, and the time interval.

2. The FE model allows to uncover details about the projectile flight characteristics (three flight phases) and driving mechanism inside the tube.

In conclusion, the experimental and numerical investigations performed in this work will prove useful in the domain of the effect of explosively driven inserts in improvised explosive devices. The laboratory experimental technique can be used for future experimental work.

Supplementary Materials: The following supporting information can be downloaded at: https://www.mdpi.com/article/10.3390/app12146854/s1, Video S1: Typical flight trajectory of a 7 mm diameter projectile attached to the front surface of a detonator after being propelled by the explosion. (https://doi.org/10.5281/zenodo.6799391); Video S2: A typical result from the high-speed camera HSC for the flight trajectory of a 7 mm diameter projectile propelled from the explosion of 10 g C4 at the entrance of the explosive driven shock tube. (https://doi.org/10.5281/zenodo.6799452); Video S3: Plate deformation and projectile perforation resulting from the explosion of 10 g of C4 at the entrance of the explosive driven shock tube. (https://doi.org/10.5281/zenodo.6799506).

Author Contributions: Conceptualization, D.L.; methodology, O.A., B.B. and A.M. (Azer Maazoun); investigation, O.A., A.M. (Abdelhafidh Moumen) and A.M. (Azer Maazoun); resources, D.L.; data curation, O.A. and A.M. (Abdelhafidh Moumen); writing—original draft preparation, O.A.; software, O.A., A.M. (Abdelhafidh Moumen) and G.K.; validation, O.A. and A.M. (Abdelhafidh Moumen); supervision, D.L. and L.P. All authors have read and agreed to the published version of the manuscript.

Funding: This research received no external funding.

Institutional Review Board Statement: Not applicable.

Informed Consent Statement: Not applicable.

Data Availability Statement: The data presented in this study are available on request from the corresponding author.

Acknowledgments: The authors are grateful to the staff of the Laboratory of Propellants, Explosives and Blast Engineering (PEBE) department of the Royal Military Academy (RMA) in Brussels for their support and assistance in performing the different steps of the experimental work.

Conflicts of Interest: The authors declare no conflict of interest.

References

1. Explosive Violence Monitor: 2020. Available online: https://aoav.org.uk/2021/explosive-violence-in-2020/ (accessed on 21 March 2022).
2. Improvised Explosive Device (IED) Monitor. Available online: https://reliefweb.int/sites/reliefweb.int/files/resources/IED-Monitor-Report-for-web-final.pdf (accessed on 21 March 2022).
3. Marchand, K.A.; Vargas, M.; Nixon, J.D. *The Synergistic Effects of Combined Blast and Fragment Loadings*; Technical Report; Southwest Research Inst.: San Antonio, TX, USA, 1992.
4. Kong, X.S.; Wu, W.G.; Li, J.; Chen, P.; Liu, F. Experimental and Numerical Investigation on a Multi-Layer Protective Structure under the Synergistic Effect of Blast and Fragment Loadings. *Int. J. Impact Eng.* **2013**, *65*, 146–162. [CrossRef]
5. Gotts, P. International ballistic and blast specifications and standards. In *Lightweight Ballistic Composites*; Elsevier: Amsterdam, The Netherlands, 2016; pp. 115–156. [CrossRef]
6. Xie, W.; Zhang, W.; Kuang, N.; Li, D.; Huang, W.; Gao, Y.; Ye, N.; Guo, L.; Ren, P. Experimental investigation of normal and oblique impacts on CFRPs by high velocity steel sphere. *Compos. Part B Eng.* **2016**, *99*, 483–493. [CrossRef]
7. Lozano, E. *Design and Analysis of a Personnel Blast Shield for Different Explosives Applications*; Colorado School of Mines: Golden, CO, USA, 2016.
8. Nurick, G.; Martin, J. Deformation of thin plates subjected to impulsive loading—A review Part II: Experimental studies. *Int. J. Impact Eng.* **1989**, *8*, 171–186. [CrossRef]
9. Maazoun, A.; Belkassem, B.; Reymen, B.; Matthys, S.; Vantomme, J.; Lecompte, D. Blast response of RC slabs with externally bonded reinforcement: Experimental and analytical verification. *Compos. Struct.* **2018**, *200*, 246–257. [CrossRef]
10. Zhu, W.; Huang, G.; Liu, H.; Lai, W.; bin Bian, X.; Shan, F.S. Experimental and numerical investigation of a hollow cylindrical water based barrier against internal blast induced fragment loading. *Int. J. Impact Eng.* **2020**, *138*, 103503. [CrossRef]
11. Grisaro, H.D.A. Towards a better understanding of the response of RC barriers to combined loading of blast and fragments. In Proceedings of the The 11th fib International PhD Symposium in Civil Engineering, Tokyo, Japan, 29–31 August 2016; pp. 353–360.

12. Zhang, C.; Cheng, Y.; Zhang, P.; Duan, X.; Liu, J.; Li, Y. Numerical investigation of the response of I-core sandwich panels subjected to combined blast and fragment loading. *Eng. Struct.* **2017**, *151*, 459–471. [CrossRef]
13. Cai, S.; Liu, J.; Zhang, P.; Li, C.; Cheng, Y.; Chen, C. Experimental study on failure mechanisms of sandwich panels with multi-layered aluminum foam/UHMWPE laminate core under combined blast and fragments loading. *Thin-Walled Struct.* **2021**, *159*, 107227. [CrossRef]
14. Grisaro, H.Y.; Dancygier, A.N. Dynamic Response of RC Elements Subjected to Combined Loading of Blast and Fragments. *Eng. Struct.* **2021**, *147*, 04020315. [CrossRef]
15. Nyström, U.; Gylltoft, K. Numerical studies of the combined effects of blast and fragment loading. *Int. J. Impact Eng.* **2009**, *36*, 995–1005. [CrossRef]
16. Zhang, C.; Gholipour, G.; Mousavi, A.A. Nonlinear dynamic behavior of simply-supported RC beams subjected to combined impact-blast loading. *Eng. Struct.* **2019**, *181*, 124–142. [CrossRef]
17. Li, Y.; Chen, Z.; Ren, X.; Tao, R.; Gao, R.; Fang, D. Experimental and numerical study on damage mode of RC slabs under combined blast and fragment loading. *Int. J. Impact Eng.* **2020**, *142*, 103579. [CrossRef]
18. Lai, E.; Zhao, J.; Li, X.; Hu, K.; Chen, G. Dynamic responses and damage of storage tanks under the coupling effect of blast wave and fragment impact. *J. Loss Prev. Process Ind.* **2021**, *73*, 104617. [CrossRef]
19. Price, M.A.; Nguyen, V.T.; Hassan, O.; Morgan, K. An approach to modeling blast and fragment risks from improvised explosive devices. *Appl. Math. Model.* **2017**, *50*, 715–731. [CrossRef]
20. Li, L.; Zhang, Q.C.; Zhang, R.; Wang, X.; Zhao, Z.Y.; He, S.Y.; Han, B.; Lu, T.J. A laboratory experimental technique for simulating combined blast and impact loading. *Int. J. Impact Eng.* **2019**, *134*, 103382. [CrossRef]
21. Qi, R.; Langdon, G.S.; Cloete, T.J.; Yuen, S.C.K. Behaviour of a blast-driven ball bearing embedded in rear detonated cylindrical explosive. *Int. J. Impact Eng.* **2020**, *146*, 103698. [CrossRef]
22. LS-DYNA Keyword User's Manual Volume I. Available online: https://lstc.com/pdf/ls-dyna_971_manual_k.pdf (accessed on 21 March 2022).
23. Mellen, P.; Shanahan, C.; Bennett, T. Blast and fragmentation loading indicative of a VBIED surrogate for structural panel response analysis. *Int. J. Impact Eng.* **2019**, *126*, 172–184. [CrossRef]
24. Louar, M.; Belkassem, B.; Ousji, H.; Spranghers, K.; Kakogiannis, D.; Pyl, L.; Vantomme, J. Explosive driven shock tube loading of aluminium plates: Experimental study. *Int. J. Impact Eng.* **2015**, *86*, 111–123. [CrossRef]
25. PCB Dynamic Pressure Sensors for High Frequency Measurements. Available online: https://www.pcb.com/Contentstore/MktgContent/LinkedDocuments/Pressure/TM-PRS-113B-102B_lowres.pdf (accessed on 21 March 2022).
26. Moumen, A.; Grossen, J.; Ndindabahizi, I.; Gallant, J.; Hendrick, P. Visualization and Analysis of Muzzle Flow Fields Using the Background-Oriented Schlieren Technique. *J. Vis.* **2020**, *23*, 409–423. [CrossRef]
27. Atoui, O.; Lecompte, D.; Belkassem, B. Tests Showing the Projectile Flight Trajectory of 5, 7 and 8 mm Diameter Steel Spheres Attached to Either a Detonator or a Rear Detonated C4 Spherical Explosive Charge. *Zenodo* **2022**, 70238. [CrossRef]
28. Robbe, C.; Nsiampa, N.; Oukara, A.; Papy, A. Quantification of the uncertainties of high-speed camera measurements. *Int. J. Metrol. Qual.* **2014**, *5*, 201. [CrossRef]
29. Robbe, C.; Nsiampa, N.; Papy, A.; Oukara, A. Practical considerations for using high-speed camera to measure dynamic deformation occurring at the impact of a kinetic energy non-lethal weapon projectile on ballistic simulant. In Proceedings of the Personal Armour System Symposium (PASS) Conference Proceedings, Nuremberg, Germany, 17–21 September 2012.
30. Thielicke, W.; Stamhuis, E.J. PIVlab—Towards User-friendly, Affordable and Accurate Digital Particle Image Velocimetry in MATLAB. *J. Open Res. Softw.* **2014**, *7*, 14. [CrossRef]
31. Photron FASTCAM Viewer Operation Manual. Available online: https://www.techimaging.com/downloads/docs/Photron_FASTCAM_Viewer_Manual_Rev2437en.pdf (accessed on 21 March 2022).
32. Langdon, G.; Curry, R.; Rigby, S.; Pickering, E.; Clarke, S.; Tyas, A. Optical diagnostics in near-field blast measurements. *Fire Blast Inf. Group Tech. Newsl.* **2021**, *82*, 25–30.
33. Peton, N.; Lardjane, N. An Eulerian version of geometrical blast dynamics for 3D simulations. *Shock Waves* **2022**, *32*, 241–259. [CrossRef]
34. Chen, M.; Liu, M.; Tang, Y. Comparison of Euler-Euler and Euler-Lagrange approaches for simulating gas-solid flows in a multiple-spouted bed. *Int. J. Chem. Reactor Eng.* **2019**, *17*, 20180254. [CrossRef]
35. Ma, T.; Wang, C.; Ning, J. Multi-material eulerian formulations and hydrocode for the simulation of explosions. *Comp. Model. Eng. Sci. CMES* **2008**, *33*, 155–178. [CrossRef]
36. Gao, C.; Kong, X.-z.; Fang, Q.; Hong, J.; Wang, Y. Numerical investigation on free air blast loads generated from center-initiated cylindrical charges with varied aspect ratio in arbitrary orientation. *Def. Technol.* **2021**. [CrossRef]
37. Schwer, L.; Rigby, S. Secondary and height of burst shock reflections: Application of afterburning. In Proceedings of the 25th International Symposium on Military Aspects of Blast and Shock, Paper, The Hague, The Netherlanders, 21–25 September 2018.
38. Ning, P.; Tang, D. Influence of explosive density on small scale internal blast experiments. *J. Chongqing Univ.* **2012**, *11*, 119–126.
39. Dobratz, B.M. *LLNL Explosives Handbook: Properties of Chemical Explosives and Explosive Simulants*; Technical Report; Lawrence Livermore National Lab.: Livermore, CA, USA, 1981.
40. Riegel, J.J.P.; Davison, D. Consistent constitutive modeling of metallic target penetration using empirical, analytical, and numerical penetration models. *Def. Technol.* **2016**, *126*, 172–184. [CrossRef]